

# Probing the exotic structure of ${}^8\text{B}$ by its elastic scattering and breakup reaction on nuclear targets

V.K. Lukyanov<sup>1</sup>, D.N. Kadrev<sup>2</sup>, E.V. Zemlyanaya<sup>1</sup>, K.V. Lukyanov<sup>1</sup>, A.N. Antonov<sup>2</sup>, M.K. Gaidarov<sup>2</sup>, and K. Spasova<sup>2,3</sup>

<sup>1</sup> Joint Institute for Nuclear Research, Dubna 141980, Russia

<sup>2</sup> Institute for Nuclear Research and Nuclear Energy, Bulgarian Academy of Sciences, Sofia 1784, Bulgaria

<sup>3</sup> University "Ep. K. Preslavski", Shumen 9712, Bulgaria

Received: date / Revised version: date

**Abstract.** The structure of the exotic  ${}^8\text{B}$  nucleus is studied by means of elastic scattering, as well as its breakup on nuclear targets. We present microscopic calculations of the optical potentials (OPs) and cross sections of elastic scattering of  ${}^8\text{B}$  on  ${}^{12}\text{C}$ ,  ${}^{58}\text{Ni}$ , and  ${}^{208}\text{Pb}$  targets at energies  $20 < E < 170$  MeV. The density distributions of  ${}^8\text{B}$  obtained within the variational Monte Carlo (VMC) model and the three-cluster model (3CM) are used to construct the potentials. The real part of the hybrid OP is calculated using the folding model with the direct and exchange terms included, while the imaginary part is obtained on the base of the high-energy approximation (HEA) and also taken to be equal to the microscopic real part of the OP. In this model the only free parameters are the depths of the real and imaginary parts of OP obtained by fitting the elastic scattering experimental data. It is found a dependence of their values on the model density of  ${}^8\text{B}$ . In addition, cluster model, in which  ${}^8\text{B}$  consists of a  $p$ -halo and the  ${}^7\text{Be}$  core, is applied to calculate the breakup cross sections of  ${}^8\text{B}$  nucleus on  ${}^9\text{Be}$ ,  ${}^{12}\text{C}$ , and  ${}^{197}\text{Au}$  targets, as well as momentum distributions of  ${}^7\text{Be}$  fragments, and a comparison with the existing experimental data is made.

**PACS.** 21.10.Gv Nucleon distributions and halo features – 24.10.Ht Optical and diffraction models

## 1 Introduction

The development of the radioactive ion beams has allowed studies of nuclei far from stability. This technical headway led to the discovery of halo nuclei on the neutron-rich side of the valley of stability [1, 2]. These weakly bound nuclei have a strongly clusterized structure [3, 4, 5, 6]. In a simple model, they are seen as a core, that contains most of the nucleons, to which one or two neutrons are loosely bound. Due to this poor binding, the valence neutrons tunnel far outside the classically allowed region and form a sort of halo around the core [7].

Although less probable, proton halos are also possible. Knowledge about the short-lived radioactive nucleus  ${}^8\text{B}$  is valuable both for astrophysical reasons [8, 9, 10] and for clarifying the question of the existence of proton halo. Many different findings of evidence argue for the latter. First, the proton separation energy of only 136.4 keV shows up that  ${}^8\text{B}$  is the most likely candidate for such a proton-halo nucleus. Second, the interaction cross section at 790 MeV/nucleon indicates that the root-mean-square (rms) radius of  ${}^8\text{B}$  is different from more tightly bound Boron isotopes [11, 12]. The relativistic mean-field calculations of the rms radii performed systematically for light isotopes ( $A < 40$ ) show that  ${}^8\text{B}$  has a large proton matter radius compared to its neutron matter radius [13]. The enhanced

reaction cross section extracted by angular distribution measurements at intermediate energies [14, 15, 16] and the large proton-removal cross section at relativistic and intermediate energies with targets ranging from carbon to lead nuclei [14, 17, 18] support a halo structure of  ${}^8\text{B}$ . A radius of the matter density of 2.7 fm, i.e., much larger than the prediction of any self-consistent calculation is shown to explain the experimental quadrupole moment of  ${}^8\text{B}$  [19, 20].

The narrow momentum distributions of  ${}^7\text{Be}$  fragments in the breakup of  ${}^8\text{B}$  measured in C, Al, and Pb targets at 1471 MeV/nucleon with full width at half maximum (FWHM) of  $81 \pm 6$  MeV/c in all targets have been interpreted in terms of a largely extended proton distribution for  ${}^8\text{B}$  and have implied a radius of 2.78 fm [21]. Here we should mention also the results of the experiments at lower energies for the breakup of  ${}^8\text{B}$  in the collisions with Be and Au targets at 41 MeV/nucleon ( $81 \pm 4$  and  $62 \pm 3$  MeV/c FWHM for Be and Au targets, respectively) [22] and for C target at 36 MeV/nucleon [23] with FWHM  $124 \pm 17$  and  $92 \pm 7$  MeV/c for the stripping and diffraction components, correspondingly. Indeed, these experimental results reflect the large spatial extension of the loosely bound proton in  ${}^8\text{B}$ . The halo nature of  ${}^8\text{B}$  nucleus through studies of its breakup has been mostly tested with cluster models pre-

suming simple two-cluster structure that consists of  ${}^7\text{Be}$  core and valence proton (for instance, Refs. [18,21,24], and Ref. [25] presenting a Fortran code to calculate cross sections for the core plus one-nucleon case) or extended three-body model ( $\alpha+{}^3\text{He}+p$ ) [26]. The latter model used to interpret the experimental data in Ref. [18], as well as quasiparticle RPA calculations [21] and Serber model applied to data in Ref. [22], demonstrate the necessity to have a rms  ${}^7\text{Be}-p$  distance of 4–4.5 fm in order to reproduce the small momentum distribution width. Such a relatively large value of the rms radius for the last proton in  ${}^8\text{B}$  ( $4.20 \pm 0.22$  fm) compared to the rms radii of the  ${}^7\text{Be}$  core and  ${}^8\text{B}$  projectile was also obtained by Carstoiu *et al.* [27] from the analysis of the experimentally measured asymptotic normalization coefficient for  ${}^8\text{B} \rightarrow {}^7\text{Be}+p$  process. However, as it has been pointed out in Ref. [21], the ground state of  ${}^8\text{B}$  is more complex than simply a proton around an inert  ${}^7\text{Be}$  core and nuclear structure calculations with an appropriate treatment of continuum effects can describe the measured narrow momentum distribution and cross sections.

The idea of the existence of a proton halo in  ${}^8\text{B}$  was experimentally verified also in measurements and studies of differential cross sections of  ${}^8\text{B}$  elastic scattering on different nuclear targets in the energy range 20–170 MeV [28,29,30]. To describe the elastic-scattering angular distributions and total reaction cross sections conventional optical-model with Woods-Saxon (WS) potentials or double-folding (DF) OPs calculations were performed. The effect of breakup on the elastic scattering was investigated for the weakly bound  ${}^8\text{B}$  nucleus by performing continuum discretized coupled-channels (CDCC) calculations [28,29,30,31,32,33,34]. It was found that for the light  ${}^{12}\text{C}$  target this effect is negligible for description of the elastic scattering data [28,31]. Similar conclusion has been drawn in Ref. [30], in which the CDCC calculations have shown a small effect of breakup channel couplings on the  ${}^8\text{B}+{}^{208}\text{Pb}$  elastic scattering at an incident energy well above the Coulomb barrier.

The aims of the present work are as follows. First, we analyze the data on elastic scattering cross sections of  ${}^8\text{B}$  on  ${}^{12}\text{C}$ ,  ${}^{58}\text{Ni}$ , and  ${}^{208}\text{Pb}$  targets at energies  $20 < E < 170$  MeV within the microscopic model of the respective OP and compare the results with the available experimental data. As in our previous works [35,36,37,38,39], where processes with neutron-rich He, Li, and Be isotopes were considered, we use the hybrid model of OP [40], in which the real part (ReOP) is calculated by a folding of a nuclear density and the effective nucleon-nucleon (NN) potentials [41] (see also [42]) and includes direct and exchange isoscalar and isovector parts. The imaginary part (ImOP) is obtained in two ways: i) on the base of the high-energy approximation method developed in Refs. [43,44] and ii) taken to be equal to microscopically calculated folding real part of the OP. There are only two fitting parameters in the hybrid model. They are related to the depths of the ReOP and ImOP. In the present work we use the density distribution obtained within the variational Monte Carlo model [45,46] and also the density

obtained within the framework of the microscopic three-cluster model of Varga *et al.* [47]. The main effort is to minimize the ambiguities in the fitted OPs by studying differential elastic cross sections and to compare them with the available experimental data, namely for reactions  ${}^8\text{B}+{}^{12}\text{C}$  at 25.8 MeV [28],  ${}^8\text{B}+{}^{58}\text{Ni}$  at 20.7, 23.4, 25.3, 27.2, and 29.3 MeV [29], and  ${}^8\text{B}+{}^{208}\text{Pb}$  at 170.3 MeV [30]. Second, in addition to the analysis of elastic scattering cross sections, we estimate important characteristics of the reactions with  ${}^8\text{B}$ , such as the breakup cross sections and momentum distributions of fragments in breakup processes on nuclear targets. For a more consistent description of the possible halo structure of  ${}^8\text{B}$  we calculate the momentum distributions of  ${}^7\text{Be}$  fragments from the breakup reactions  ${}^8\text{B}+{}^9\text{Be}$ ,  ${}^8\text{B}+{}^{12}\text{C}$ , and  ${}^8\text{B}+{}^{197}\text{Au}$  for which experimental data are available. Such a complex study based on the microscopic method to obtain the OPs with a minimal number of free parameters and by testing density distributions of  ${}^8\text{B}$  which reflect its proton-halo structure (in contrast, e.g., to the Hartree-Fock density used in Ref. [30]) would lead to a better understanding of the  ${}^8\text{B}$  structure and to a reduction of the inconsistency of describing the available data. Also, it would be a test of our microscopic approach to reveal the proton-halo structure of the loosely bound  ${}^8\text{B}$  projectile, particularly its density distribution, in the considered elastic scattering and breakup processes.

The article is organized as follows. The theoretical scheme to calculate the real and imaginary parts of the OP, as well as the results for the  ${}^8\text{B}+{}^{12}\text{C}$ ,  ${}^8\text{B}+{}^{58}\text{Ni}$ , and  ${}^8\text{B}+{}^{208}\text{Pb}$  elastic scattering differential cross sections are presented and discussed in Sec. 2. Section 3 contains the basic expressions to estimate the  ${}^8\text{B}$  breakup and results for the fragment momentum distributions of  ${}^7\text{Be}$  in the stripping process of  ${}^8\text{B}$  on  ${}^9\text{Be}$ ,  ${}^{12}\text{C}$ , and  ${}^{197}\text{Au}$ . The summary of the work and conclusions are given in Sec. 4.

## 2 Elastic scattering of ${}^8\text{B}$ on ${}^{12}\text{C}$ , ${}^{58}\text{Ni}$ , and ${}^{208}\text{Pb}$

### 2.1 The microscopic optical potential

The microscopic volume OP used in our calculations contains the real part ( $V^{DF}$ ) including both the direct and exchange terms and the HEA microscopically calculated imaginary part ( $W^H$ ). It has the form

$$U(r) = N_R V^{DF}(r) + i N_I W^H(r). \quad (1)$$

The parameters  $N_R$  and  $N_I$  entering Eq. (1) renormalize the strength of OP and are fitted by comparison with the experimental cross sections. Details of the constructing of the OP are given in Refs. [41,42,48,49]. The real part  $V^{DF}$  consists of the direct ( $V^D$ ) and exchange ( $V^{EX}$ ) double-folding integrals that include effective  $NN$  potentials and density distribution functions of colliding nuclei. The  $V^D$  and  $V^{EX}$  parts of the ReOP have isoscalar (IS) and isovector (IV) contributions. The IS ones of both terms are:

$$V_{IS}^D(r) = \int d^3r_p d^3r_t \rho_p(\mathbf{r}_p) \rho_t(\mathbf{r}_t) v_{NN}^D(s), \quad (2)$$

$$V_{IS}^{EX}(r) = \int d^3r_p d^3r_t \rho_p(\mathbf{r}_p, \mathbf{r}_p + \mathbf{s}) \rho_t(\mathbf{r}_t, \mathbf{r}_t - \mathbf{s}) \times v_{NN}^{EX}(s) \exp\left[\frac{i\mathbf{K}(r) \cdot \mathbf{s}}{M}\right], \quad (3)$$

where  $\mathbf{s} = \mathbf{r} + \mathbf{r}_t - \mathbf{r}_p$  is the vector between two nucleons, one of which belongs to the projectile and another one to the target nucleus. In Eq. (2)  $\rho_p(\mathbf{r}_p)$  and  $\rho_t(\mathbf{r}_t)$  are the densities of the projectile and the target, respectively, while in Eq. (3)  $\rho_p(\mathbf{r}_p, \mathbf{r}_p + \mathbf{s})$  and  $\rho_t(\mathbf{r}_t, \mathbf{r}_t - \mathbf{s})$  are the density matrices for the projectile and the target that are usually taken in an approximate form [50]. The effective  $NN$  interactions  $v_{NN}^D$  and  $v_{NN}^{EX}$  have their IS and IV components in the form of M3Y interaction obtained within  $g$ -matrix calculations using the Paris NN potential [41]. The expressions for the energy and density dependence of the effective  $NN$  interaction are given, e.g., in Ref. [39].

It is important to note that the energy dependence of  $V^{EX}$  arises primarily from the contribution of the exponent in the integrand of Eq. (3). Indeed, there the local nucleus-nucleus momentum reads

$$K(r) = \left\{ \frac{2Mm}{\hbar^2} [E - V^{DF}(r) - V_c(r)] \right\}^{1/2} \quad (4)$$

with  $M = A_p A_t / (A_p + A_t)$ , where  $A_p$ ,  $A_t$ ,  $m$  are the projectile and target atomic numbers and the nucleon mass. As can be seen,  $K(r)$  depends on the folding potential  $V^{DF}(r)$  that has to be calculated itself and, therefore, we have to deal with a typical non-linear problem.

Concerning the ImOP, we take it in two forms. One of them corresponds to the full microscopic OP derived in Refs. [40,51] within the HEA [43,44]:

$$W^H(r) = -\frac{1}{2\pi^2} \frac{E}{k} \bar{\sigma}_N \times \int_0^\infty j_0(qr) \rho_p(q) \rho_t(q) f_N(q) q^2 dq. \quad (5)$$

In Eq. (5)  $\rho(q)$  are the corresponding form factors of the nuclear densities,  $f_N(q)$  is the amplitude of the NN scattering and  $\bar{\sigma}_N$  is the averaged over the isospin of the nucleus total NN scattering cross section that depends on the energy and accounts for the in-medium effect [52,53,54]. The second form of  $W$  is equal to the microscopically calculated folding real part  $V^{DF}$  of the OP.

## 2.2 Results of calculations of elastic scattering cross sections

We calculate the OP [Eq. (1)] and the elastic scattering differential cross sections of  ${}^8\text{B}$  on different targets using the DWUCK4 code [55]. All the elastic scattering cross sections will be shown in the figures as ratios to the Rutherford cross section.

To apply the microscopic OPs to scattering of  ${}^8\text{B}$  on nuclei we used realistic density distributions of  ${}^8\text{B}$  calculated within the VMC model [45,46] and from the 3CM

in Ref. [47]. In our case, within the VMC method the proton and neutron densities have been computed with the AV18+UX Hamiltonian, in which the Argonne v18 two-nucleon and Urbana X three-nucleon potentials are used [46]. Urbana X is intermediate between the Urbana IX and Illinois-7 models (the latter was used by us in Ref. [39] for the densities of  ${}^{10}\text{Be}$  nucleus). As far as the 3CM densities of Varga *et al.* [47] are concerned, the  ${}^8\text{B}$  nucleus has been studied in a microscopic  $\alpha+h+p$  three-cluster model ( $h={}^3\text{He}$ ) using the stochastic variational method, where a Minnesota effective two-nucleon interaction composed from central and spin-orbit parts was used. It has been shown in [47] that the proton separation energy of  ${}^8\text{B}$  is reasonably reproduced, but the calculated point matter radius exceeds the "empirical" one. The VMC and 3CM densities are given in Fig. 1. It can be seen that they have been calculated with enough accuracy up to distances much larger than the nuclear radius. In both methods the total densities of  ${}^8\text{B}$  occur quite similar up to  $r \sim 4$  fm and a difference between them is seen in their periphery. Due to the cluster-structure model of  ${}^8\text{B}$ , where the proton is considered as a single cluster [47], the tail part of the point-proton distribution of  ${}^8\text{B}$  is significantly larger than that of the neutron one, causing considerable difference in the corresponding rms radii listed in Table 1. In it we give also the "empirical" data, e.g. from Refs. [11,15], for the effective rms radii of the point-proton, point-neutron and matter distributions deduced from the Glauber analysis of the interaction and reaction cross sections. One can see from Table 1 that the values of the proton and matter rms radii in the case of VMC density are close to the "empirical" values for  ${}^8\text{B}$ , while the neutron radius obtained in the 3CM almost coincides with the experimental value. In the calculations of the OPs for  ${}^8\text{B}+{}^{12}\text{C}$  the density of  ${}^{12}\text{C}$  was taken in symmetrized Fermi form with radius and diffuseness parameters 3.593 fm and 0.493 fm [56], respectively. For  ${}^8\text{B}+{}^{58}\text{Ni}$  and  ${}^8\text{B}+{}^{208}\text{Pb}$  elastic scattering the densities of  ${}^{58}\text{Ni}$  and  ${}^{208}\text{Pb}$  were taken in a form of two-parameter Fermi distributions with radius and diffuseness parameters 4.08 fm and 0.515 fm [41], 6.654 fm and 0.475 fm [57], respectively.

The real part of the OPs in the considered cases are calculated using Eqs. (1)-(4). The imaginary part of the OPs is obtained in two ways: i)  $W = W^H$ , where  $W^H$  is from Eq. (5), or ii) taken to be equal to the real part of the OP ( $W = V^{DF}$ ). It is seen from our results that the different behavior of the two densities (VMC and 3CM) used in the OPs calculations reflects on the shape of the ReOP and ImOP in their periphery being with a longer tail for 3CM density. At the same time (e.g., in the case of  ${}^8\text{B}+{}^{58}\text{Ni}$  elastic scattering), the imaginary parts of the OPs calculated in HEA and corresponding to both  ${}^8\text{B}$  densities are almost one order of magnitude deeper than the real parts. It is clear that this behavior of the central part of the HEA ImOP is not realistic. From other side, however, it is known that the decisive region of the OP at such energies is the surface one. So, our further calculations of the elastic cross sections explore namely the role of the surface component of the OP. Further in our

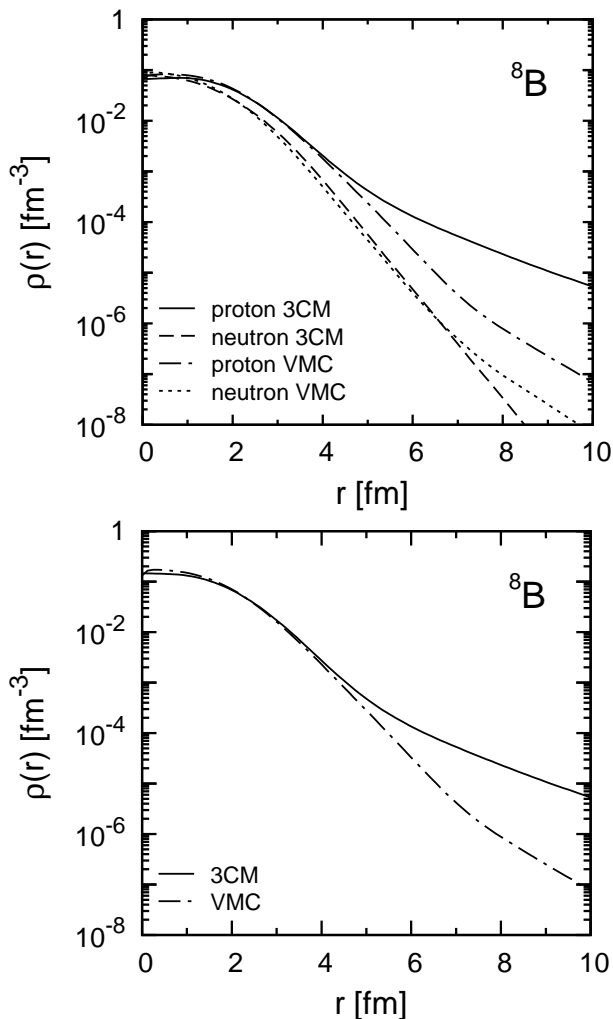


**Fig. 1.** Point-proton (normalized to  $Z=5$ ), point-neutron (normalized to  $N=3$ ) (top panel) and the total densities (bottom panel) of  ${}^8\text{B}$  (normalized to  $A=8$ ) obtained in the VMC [45, 46] method and in the 3CM [47].

**Table 1.** Proton, neutron, and matter rms radii (in fm) of  ${}^8\text{B}$  obtained within the VMC method [46] and 3CM [47]. The “empirical” effective rms radii are from Refs. [11, 15].

	$r_p$	$r_n$	$r_m$
VMC	2.45	2.14	2.34
3CM	2.73	2.24	2.56
[11]	2.45	2.27	2.38
[15]	2.53	2.31	2.45

work we show, as an example (see Fig. 7), our results that confirm this fact. We note, as it has been pointed out in Ref. [29], that every acceptable potential has an imaginary part that is extended beyond the corresponding real part. As a result, an absorption at a large distance due to the existence of a halo state is suggested.

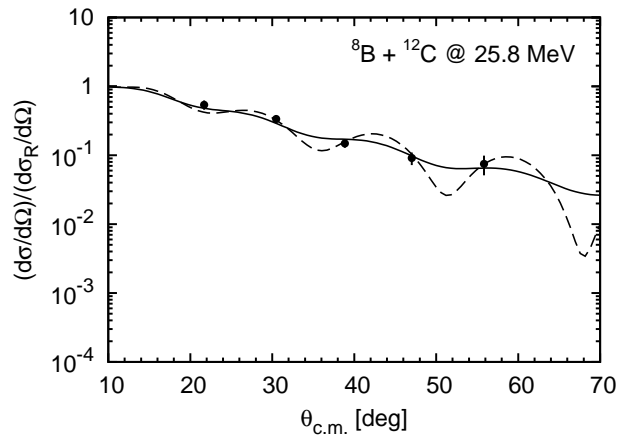


**Fig. 2.**  ${}^8\text{B}+{}^{12}\text{C}$  elastic scattering cross sections at  $E = 25.8$  MeV. Solid line: calculations with 3CM density of  ${}^8\text{B}$ ; dashed line: calculations with VMC density of  ${}^8\text{B}$ . Experimental data are taken from Ref. [28].

In our work we consider the set of the  $N_i$  coefficients ( $N_R$  and  $N_I$ , see Eq. (1) for the OP) as parameters to be found out from the fit to the experimental data for the cross sections using the  $\chi^2$ -procedure. We should mention (as it had been emphasized in our previous works [35, 36, 37, 38, 39]) that we do not aim to find a complete agreement with the data. The fitted  $N$ s related to the depths of the ReOP and ImOP can be considered as a measure of deviations of our microscopic OPs from the case when the values of  $N$ s are equal to unity.

The calculated within the hybrid model elastic scattering cross sections of  ${}^8\text{B}+{}^{12}\text{C}$  at energy  $E = 25.8$  MeV in the laboratory frame are given in Fig. 2 and compared with the experimental data [28]. It can be seen that in both cases of calculations with VMC or 3CM densities the results are in good agreement with the available data. The differential cross section obtained with VMC density demonstrates more developed diffractive picture. It would be desirable to measure the elastic scattering in the angular range beyond  $55^\circ$ , where the differences between the theoretical results start, in order to determine the advantage of using VMC or 3CM microscopic densities of  ${}^8\text{B}$ . Complementary measurements at smaller steps of scattering angle would also allow one to observe some possible oscillations of the cross section. Our results reproduce the experimental data better than the analysis of the data [28] with optical-model calculations using São Paulo potential with energy dependence and nonlocality correction [58]. The imaginary part of the latter potential has the same form factor as the real part that has not been renormalized ( $N_R = 1$ ), but with a normalization of  $N_I = 0.78$ . The corresponding values of  $N_R$  and  $N_I$  parameters obtained in our work for 3CM and VMC densities, as well as the total reaction cross sections  $\sigma_R$  (in mb) are listed in Table 2.

Our next step is to study  ${}^8\text{B}$  elastic scattering on a lead target at 170.3 MeV incident energy. Although the experiment was performed with a natural lead target [30], we calculate the angular distribution as it has been also the-

**Table 2.** The renormalization parameters  $N_R$ ,  $N_I$ , and the total reaction cross sections  $\sigma_R$  (in mb) for results of the  ${}^8\text{B}+{}^{12}\text{C}$  and  ${}^8\text{B}+{}^{208}\text{Pb}$  elastic scattering processes at incident energy  $E$  (in MeV) considered and shown in Figs. 2 and 3 using the 3CM and VMC model densities of  ${}^8\text{B}$ , respectively.

Process	Model	$E$	$N_R$	$N_I$	$\sigma_R$
${}^8\text{B}+{}^{12}\text{C}$	3CM	25.8	1.075	0.433	1507.63
	VMC		2.200	0.165	1251.90
${}^8\text{B}+{}^{208}\text{Pb}$	3CM	170.3	0.661	0.389	3226.73
	VMC		1.358	0.908	3158.15

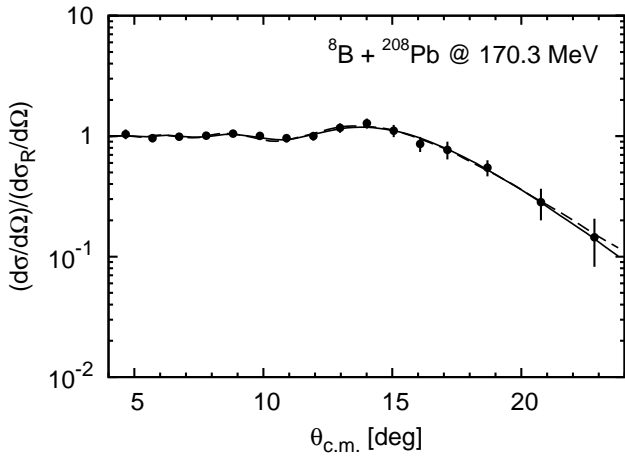


**Fig. 3.**  ${}^8\text{B}+{}^{208}\text{Pb}$  elastic scattering cross sections at  $E = 170.3$  MeV. Solid line: calculations with 3CM density of  ${}^8\text{B}$ ; dashed line: calculations with VMC density of  ${}^8\text{B}$ . Experimental data are taken from Ref. [30].

oretically interpreted in Ref. [30] assuming a pure  ${}^{208}\text{Pb}$  target. Fig. 3 shows a fair agreement of our microscopic calculations with the experimental data for the cross section. Both VMC and 3CM densities used in the calculations are able to reproduce the data that are restricted in a range of small angles. The values of  $N_R$  and  $N_I$  are given in Table 2. One can mention that the optical model analysis performed in Ref. [30] on the base of a single-folding model using the Bruyères Jeukenne-Lejeune-Mahaux nucleon-nucleus potential leads also to a fairly good agreement with experimental data. Similarly to the case of  ${}^8\text{B}+{}^{12}\text{C}$  reaction illustrated in Fig. 2, the reasonable agreement of our model with the data on  ${}^8\text{B}+{}^{208}\text{Pb}$  elastic scattering is in favor of the very weak contribution from other reaction mechanisms, which is supported by the results from CDCC calculations [28, 30, 31].

In what follows, we present in Figs. 4 and 5 our results for  ${}^8\text{B}+{}^{58}\text{Ni}$  elastic scattering cross sections at energies 20.7, 23.4, 25.3, 27.2, and 29.3 MeV using the VMC and 3CM densities, respectively. These results are obtained with  $N_R$  and  $N_I$  which reproduce in a best way the experimental cross sections at considered five energies. Their values from the fitting procedure providing minimal  $\chi^2/N$

**Table 3.** The renormalization parameters  $N_R$ ,  $N_I$ , and the total reaction cross sections  $\sigma_R$  (in mb) for results of the  ${}^8\text{B}+{}^{58}\text{Ni}$  elastic scattering at five incident energies  $E$  (in MeV) shown in Figs. 4 and 5 using the VMC and 3CM model densities of  ${}^8\text{B}$ , respectively.

Model	$E$	$N_R$	$N_I$	$\sigma_R$
VMC	20.7	0.863	2.792	208.69
3CM		0.427	0.393	201.99
VMC	23.4	0.359	1.500	376.08
3CM		0.319	0.266	370.04
VMC	25.3	0.317	1.030	494.86
3CM		0.235	0.212	480.38
VMC	27.2	0.329	1.750	794.03
3CM		0.293	0.252	705.38
VMC	29.3	0.525	1.830	987.29
3CM		0.221	0.248	847.11

are presented in Table 3. One can see that the results obtained using both densities of  ${}^8\text{B}$  are in a good agreement with the data for all energies considered. The values of the renormalization parameters  $N_R$  are smaller than the ones deduced for the  ${}^8\text{B}+{}^{12}\text{C}$  and  ${}^8\text{B}+{}^{208}\text{Pb}$  elastic scattering processes (see Table 2), in particular when using 3CM density, but the choice of the parameters is based on the same consistent  $\chi^2$  criterion. Here we would like to note that in many cases of describing real data, the elastic scattering results are not enough to determine in a unique way the parameters  $N_R$  and  $N_I$ . It is well known that the couplings to non-elastic channels lead to polarization potentials that can considerably modify the bare potential calculated within the double folding formalism. Obviously, for more successful description of cross sections at low energies near Coulomb barrier an inclusion of polarization contributions due to virtual excitations and decay channels of the reactions (involving also the fusion data Ref. [59] to explain correctly the presence of the breakup threshold anomaly for  ${}^8\text{B}+{}^{58}\text{Ni}$  process) is necessary to obtain unambiguously the OP renormalization parameters. The good fit obtained for the experimental angular distributions in Ref. [29] with real and imaginary potentials of the Woods-Saxon type and our best fit to the same data using microscopic OP in this work lead to values of the predicted total reaction cross section  $\sigma_R$  very close to each other, the latter exhibiting a smooth increase with the energy increase. The good agreement of our results for  ${}^8\text{B}+{}^{58}\text{Ni}$  elastic scattering cross sections with the experimental data using both VMC and 3CM densities validates their ability as a reasonable choice to reveal the proton-halo structure of  ${}^8\text{B}$  nucleus.

Further, we give in Fig. 6, as an example (for  $E = 29.3$  MeV), the comparison of the obtained real and imaginary parts of the OPs for both 3CM and VMC densities with the corresponding parts of the fitted Woods-Saxon potential [29]. The values of our parameters  $N_R$  and  $N_I$  are those from Table 3. Here we mention that at such energies the surface part of the ImOP plays a decisive role on the

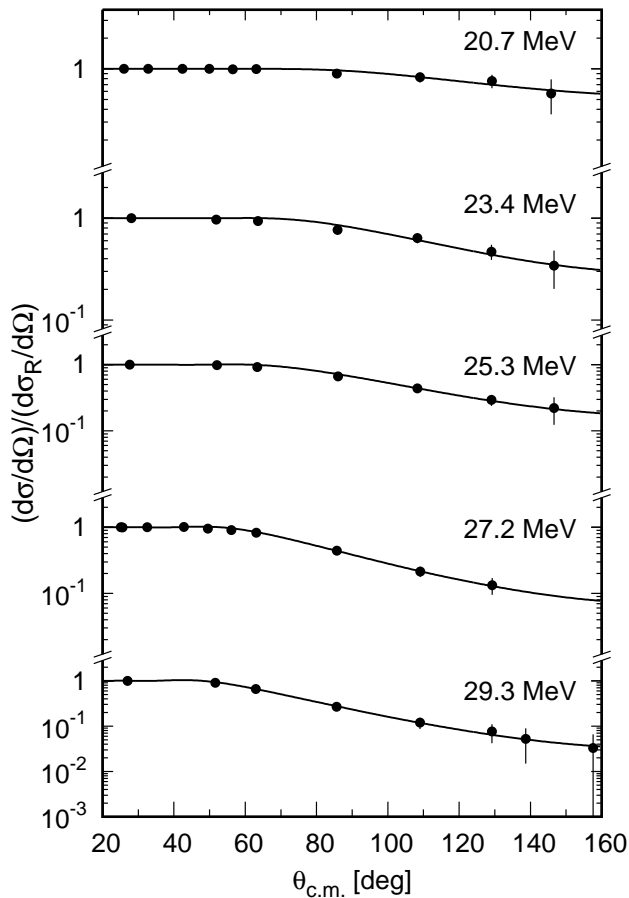


**Fig. 4.**  ${}^8\text{B}+{}^{58}\text{Ni}$  elastic scattering cross sections at  $E = 20.7, 23.4, 25.3, 27.2$  and  $29.3$  MeV calculated using the VMC density of  ${}^8\text{B}$ . Experimental data are taken from Ref. [29].

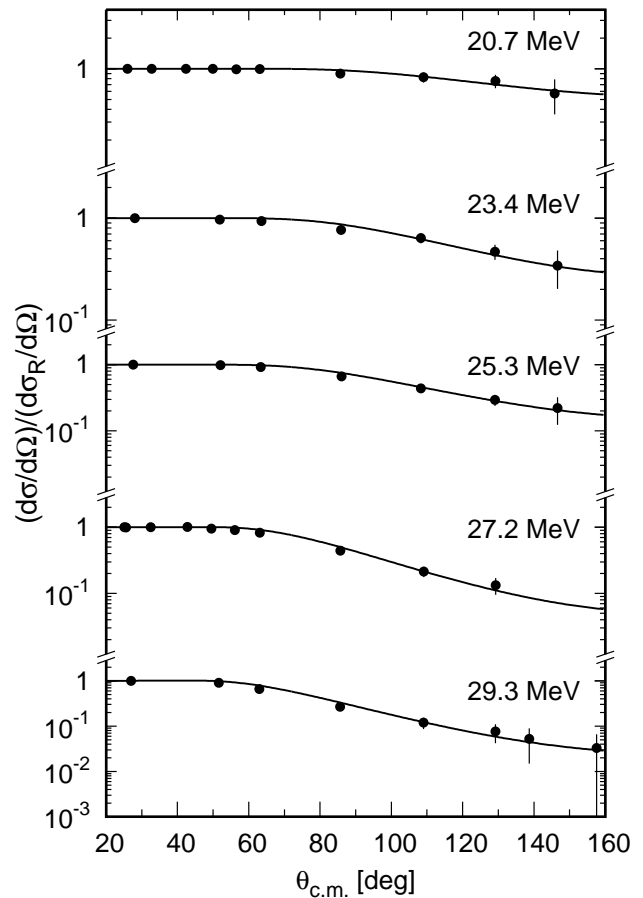


**Fig. 5.** The same as in Fig. 4 but using the 3CM density of  ${}^8\text{B}$ .

behavior of the elastic cross sections. One can see from Fig. 6 that the use of the VMC density leads to a very good agreement of the imaginary part of our OP with the imaginary part of the fitted WS OP in the surface region. Also, the slope of the real part of OP obtained with the VMC density in this region ( $8 < r < 10$  fm) is similar to that of the real part of WS OP. There exist some differences in the surface region for the real and imaginary parts of the OP obtained with the 3CM density and the corresponding parts of the WS OP.

Along this line, we present in Fig. 7 the results of another calculation, namely of the elastic  ${}^8\text{B}+{}^{58}\text{Ni}$  cross section (e.g., at energy  $E = 20.7$  MeV). The three curves correspond to the real part of the OP  $V^{DF}$  from the double folding procedure, while the ImOP is calculated in three ways: i) from HEA ( $W = W^H$ ); ii) equal to the real part of the OP ( $W = V^{DF}$ ), and iii) the central part of the ImOP is taken to be in a form of a WS potential up to  $r = 7$  fm, while the surface component of the ImOP (at  $r > 7$  fm) is taken to be equal to that from HEA ( $W = W^H$ ). The parameters of WS potential are given in Table I of Ref. [29] and its depth at  $r = 0$  fm is around two times smaller than  $V^{DF}(r = 0)$ . It can be seen that all three curves are close to each other that shows the importance

of the surface part of the OP which is similar in all three cases. In this way, in the further considerations we do not pay attention to the non-realistic values of the central part of the HEA ImOP ( $W = W^H$ ) and are concentrated on the surface component of this potential.

In the context of the obtained results for the  ${}^8\text{B}+{}^{58}\text{Ni}$  elastic scattering at near-Coulomb barrier energies, we would like also to mention the contributions of other mechanisms that play a crucial role. Lubian *et al.* showed in Ref. [32] that taking into account the coupling between elastic and breakup channels, the CDCC calculations reproduce very well the data of Ref. [29]. Although the inclusion of continuum-continuum couplings were essential to have a good agreement with the data, it was noted that nuclear excitations of the target have a weak influence on the elastic angular distributions. In addition, the analysis carried out in Ref. [59] led to a conclusion that the breakup threshold anomaly is present for the  ${}^8\text{B}+{}^{58}\text{Ni}$  system at energies close to the Coulomb barrier ( $V_B = 20.8$  MeV). So, all these findings support the important role played by the Coulomb-nuclear interference at large distances for a halo nucleus as  ${}^8\text{B}$ .

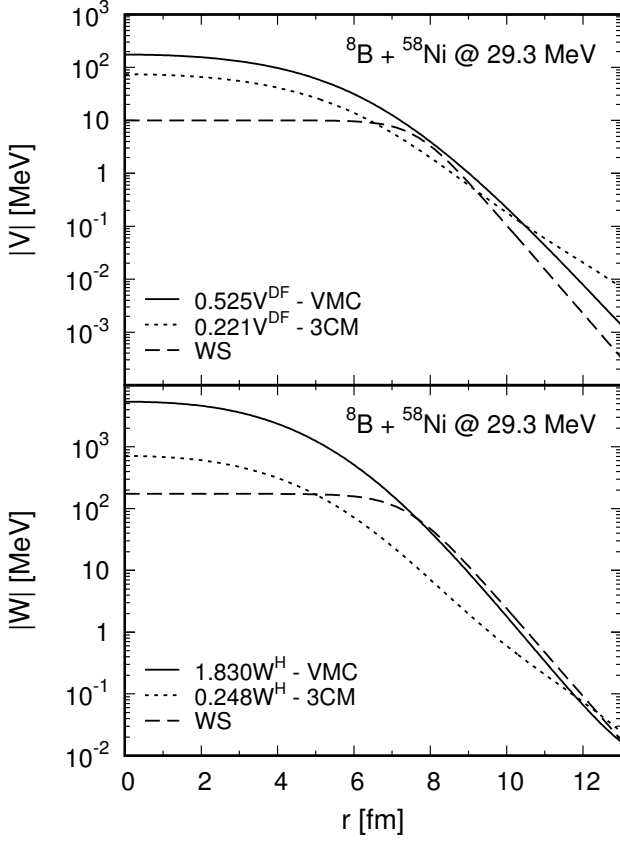


**Fig. 6.** The absolute values of the real  $N_R V^{DF}$  and imaginary  $N_I W^H$  parts of the calculated optical potentials for the  ${}^8\text{B}+{}^{58}\text{Ni}$  elastic scattering at  $E = 29.3$  MeV obtained using the VMC and 3CM densities of  ${}^8\text{B}$  in comparison with those of the WS potential from Ref. [29]. The values of  $N_R$  and  $N_I$  are from Table 3.

### 3 Breakup reactions of ${}^8\text{B}$

#### 3.1 The ${}^7\text{Be}+p$ model of ${}^8\text{B}$

In this section we consider the characteristics of breakup processes of the  ${}^8\text{B}$  nucleus on the example of the stripping reaction cross sections and the momentum distributions of the fragments. We use a simple model in which  ${}^8\text{B}$  consists of a core of  ${}^7\text{Be}$  and a halo of a single proton (see, e.g., Refs. [18,21]). In this model the density of  ${}^7\text{Be}$  has to be known. We use that one obtained from the calculations performed by means of the 3CM density of  ${}^8\text{B}$  [47]. Later in this subsection we give the expressions how to obtain the corresponding  $S$ -matrices needed to calculate the breakup cross sections through the imaginary part of cluster-target OPs within the HEA. The wave function of the relative motion of the proton and  ${}^7\text{Be}$  clusters in  ${}^8\text{B}$  is obtained by solving the Schrödinger equation with the Woods-Saxon potential for a particle with a reduced mass of two clusters. The parameters of the WS potentials are obtained by a fitting procedure, namely, to reach the proton separation energy  $S_p = 137$  KeV. However, this procedure could provide several sets of potential parameters that satisfy the above condition. They are close

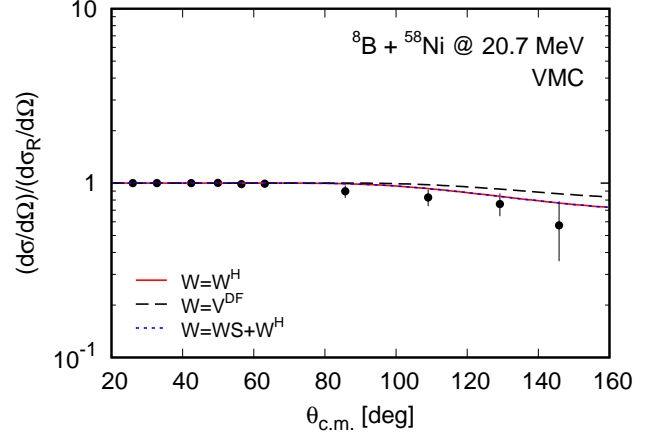


**Fig. 7.**  ${}^8\text{B}+{}^{58}\text{Ni}$  elastic scattering cross sections at  $E = 20.7$  MeV calculated using the VMC density of  ${}^8\text{B}$ . Red solid line:  $W = W^H$ ; black dashed line:  $W = V^{DF}$ ; blue dotted line:  $W = WS + W^H$  (see also the text). Experimental data are taken from Ref. [29].

**Table 4.** The parameters  $V_0$  (in MeV),  $R$  (in fm),  $a$  (in fm) of the Woods-Saxon potentials and the rms radii of the cluster wave function (in fm) obtained by using of the 3CM density of  ${}^7\text{Be}$  for three cases (see the text).

$V_0$	$R$	$a$	rms radii
38.22	2.70	0.55	4.51
38.70	2.50	0.20	5.08
38.77	2.48	0.50	6.24

to each other leading, at the same time, to different valence proton rms radii. Therefore, in order to understand better the observed widths of the longitudinal momentum distributions of  ${}^7\text{Be}$  fragments formed in the breakup of  ${}^8\text{B}$  and measured at different targets and energies, we consider three cases. The values of WS potential parameters and corresponding rms radii of the cluster formation for  $1p$  state in which the valence proton in  ${}^8\text{B}$  is mainly bound (see Refs. [60,24]) are listed in Table 4.

The wave function of the  $p$ -state ( $l = 1$ ) of the relative motion of two clusters has the form

$$\phi_{1m}(\mathbf{s}) = R_1(s)Y_{1m}(\theta, \varphi), \quad (6)$$

where  $R_1(s)$  is the radial wave function and  $Y_{1m}(\theta, \varphi)$  are the spherical functions for  $l = 1$ . The corresponding probability density of both clusters to be at a mutual distance  $s$  is written as

$$\rho_0(\mathbf{s}) = \frac{1}{4\pi} |\phi_{1m}(\mathbf{s})|^2. \quad (7)$$

For calculations of breakup cross sections and momentum distributions of fragments in the  ${}^7\text{Be}+p$  breakup model within the eikonal formalism (see, e.g. Ref. [60]), one needs the expressions of the  $S$ -matrix (as a function of the im-

parameter  $b$ ):

$$S(b) = \exp \left[ -\frac{i}{\hbar v} \int_{-\infty}^{\infty} U^{(b)}(\sqrt{b^2 + z^2}) dz \right], \quad (8)$$

where

$$U^{(b)} = V + iW \quad (9)$$

is the OP of the breakup of  ${}^8\text{B}$  in its collision with nuclear targets within the  ${}^7\text{Be}+p$  cluster model. Correspondingly (for negative  $W$ ), one can write

$$|S(b)| = \exp \left[ -\frac{1}{\hbar v} \int_{-\infty}^{\infty} |W| dz \right]. \quad (10)$$

$|S(b)|^2$  gives the probability that after the collision with a target nucleus ( $z \rightarrow \infty$ ), the cluster  $c$  or the proton with impact parameter  $b$  remains in the elastic channel ( $i = c, p$ ):

$$|S_i(b)|^2 = \exp \left[ -\frac{2}{\hbar v} \int_{-\infty}^{\infty} dz |W_i(\sqrt{b^2 + z^2})| \right], \quad (11)$$

where  $W_c$  and  $W_p$  are the imaginary parts of the OP (9) of  ${}^7\text{Be}+A$  and  $p+A$  scattering, respectively. They are calculated microscopically using the procedure given in Subsec. 2.1. The probability a cluster to be removed from the elastic channel is  $(1 - |S|^2)$ . The probability of the case when both clusters ( $c$  and  $p$ ) leave the elastic channel is  $(1 - |S_p|^2)(1 - |S_c|^2)$ .

The longitudinal momentum distribution of  ${}^7\text{Be}$  fragments produced in the breakup of  ${}^8\text{B}$  in the case of stripping reaction (when the proton leaves the elastic channel) is

$$\left( \frac{d\sigma}{dk_L} \right)_{str} = \frac{1}{3} \int_0^\infty b_p db_p [1 - |S_p(b_p)|^2] \times \int \rho d\rho d\varphi_\rho |S_c(b_c)|^2 \sum_{m=0, \pm 1} F_m(\rho), \quad (12)$$

where

$$F_m(\rho) = \left| \int_{-\infty}^{\infty} dz \exp(-ik_L z) Y_{1m}(\theta, \varphi) R_1(r) \right|^2. \quad (13)$$

After substituting the spherical functions  $Y_{1m}(\theta, \varphi)$  in Eq. (13) one obtains the following expressions

$$F_0 = \frac{3}{\pi} \left[ \int_0^\infty dz \sin(k_L z) \frac{z}{\sqrt{\rho^2 + z^2}} R_1(\sqrt{\rho^2 + z^2}) \right]^2, \quad (14)$$

$$F_1 = F_{+1} = F_{-1} = \frac{3}{2\pi} \left[ \int_0^\infty dz \cos(k_L z) \frac{\rho}{\sqrt{\rho^2 + z^2}} R_1(\sqrt{\rho^2 + z^2}) \right]^2 \quad (15)$$

Equation (12) is obtained when the incident nucleus has spin equal to zero and for the  $p$ -state of the relative motion

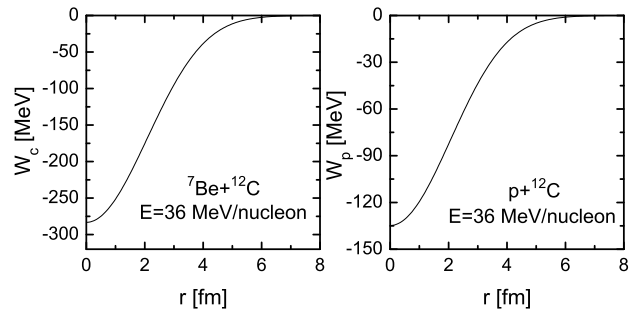


**Fig. 8.** Imaginary parts  $W_c$  and  $W_p$  of cluster-target potentials for calculation of  ${}^8\text{B}$  breakup on  ${}^{12}\text{C}$  target at  $E=36$  MeV/nucleon.

of two clusters in the nucleus with  $\mathbf{s} = \mathbf{r}_c - \mathbf{r}_p$ ,  $\rho = \mathbf{b}_c - \mathbf{b}_p$ ,  $\mathbf{s} = \rho + \mathbf{z}$  and

$$b_c = \sqrt{s^2 \sin^2 \theta + b_p^2 + 2sb_p \sin \theta \cos(\varphi - \varphi_p)} \quad (16)$$

coming from  $\mathbf{b}_c = \mathbf{b}_p + \mathbf{b}$ , where  $b = s \sin \theta$  is the projection of  $\mathbf{s}$  on the plane normal to the  $z$ -axis along the straight-line trajectory of the incident nucleus.

### 3.2 Results of calculations of breakup reactions

In this subsection we perform calculations of the breakup cross sections of  ${}^8\text{B}$  on the target nuclei  ${}^9\text{Be}$ ,  ${}^{12}\text{C}$ , and  ${}^{197}\text{Au}$  and compare our results with the available experimental data [22, 23]. The densities of these nuclei needed to compute the OPs are taken from Ref. [46] for  ${}^9\text{Be}$ , Ref. [56] for  ${}^{12}\text{C}$ , and Ref. [57] for  ${}^{197}\text{Au}$ , respectively.

In our work, to calculate the corresponding  $S$ -matrices [Eqs. (10) and (11)] one needs only the imaginary part of cluster-target potentials to be known. As an example, we illustrate in Fig. 8 the imaginary parts of both  ${}^7\text{Be}+{}^{12}\text{C}$  and  $p+{}^{12}\text{C}$  OPs calculated microscopically in HEA by using Eq. (5) within the cluster model. The results given in Fig. 8 are obtained at the same energy of 36 MeV/nucleon as the longitudinal momentum distributions of  ${}^7\text{Be}$  fragments in the breakup of  ${}^8\text{B}$  on a carbon target have been measured [23]. It is worth noting that although there are no  ${}^7\text{Be}+{}^{12}\text{C}$  and  ${}^8\text{B}+{}^{12}\text{C}$  elastic scattering data available at this specific energy, the diffraction nuclear model developed in Ref. [61] reproduces the elastic scattering of projectile exotic nuclei  ${}^7\text{Be}$  and  ${}^8\text{B}$  by  ${}^{12}\text{C}$  at similar energy (40 MeV/nucleon) [62]. In [61] the interaction of  ${}^7\text{Be}$  as a formation of two clusters ( $\alpha+{}^3\text{He}$ ) is accounted for explicitly. If measurements of the cluster-target ( ${}^7\text{Be}+{}^{12}\text{C}$  and  $p+{}^{12}\text{C}$ ) elastic scattering at energy 36 MeV/nucleon exist, one should provide additional information on the properties not only of the imaginary parts of the corresponding core-target and proton-target potentials (shown in Fig. 8), but also of their real parts (although they are not needed to calculate the breakup processes in the present work).

The stripping cross sections (when a proton leaves the elastic channel) for reactions  ${}^8\text{B}+{}^9\text{Be}$ ,  ${}^8\text{B}+{}^{12}\text{C}$ , and  ${}^8\text{B}+{}^{197}\text{Au}$  are calculated from Eq. (12). The obtained results are illustrated in Figs. 9, 10, and 11, respectively. The

blue dotted, black solid, and red dashed curves in the figures correspond to the three sets of WS parameters given in Table 4. Here we note that due to the arbitrary units of the measured cross sections of the considered processes it was not necessary to renormalize the depths of our OPs of the fragments-target nuclei interactions. It is worth to note the relevance between the rms radii of the wave function of the  ${}^7\text{Be}$ - $p$  relative motion and the obtained FWHMs for the considered three cases. The latter are presented in Table 5 together with their experimental values. Due to the uncertainty principle the widths become smaller with the increase of the distance between two clusters. We note the good agreement with the experimental data from light and heavy breakup targets. It can be seen from Figs. 9 and 10 that the best agreement with the experimental data for the parallel momentum distributions of  ${}^7\text{Be}$  fragments in a breakup reaction of  ${}^8\text{B}$  on a  ${}^9\text{Be}$  target at 41 MeV/nucleon and on a  ${}^{12}\text{C}$  target at 36 MeV/nucleon is achieved when the relative  ${}^7\text{Be}$ -proton distance is 5.08 fm or 4.51 fm, respectively, while in the case of  ${}^8\text{B}$  breakup on a  ${}^{197}\text{Au}$  target at 41 MeV/nucleon shown in Fig. 11 a larger distance (6.24 fm) is needed to get better coincidence with the data. This observation is proved by the performed  $\chi^2$  analysis for the deviation of the theoretical results from the data. The necessity to take into account the Coulomb distortion of straight-line trajectories for the heavier nucleus when calculating phases in Eqs. (10) and (11) is a reason for getting larger distance in the case of  ${}^8\text{B}$  breakup on a  ${}^{197}\text{Au}$  target. The obtained FWHMs that correspond to these rms radii listed in Table 4 are close to the experimentally measured widths. In addition, our FWHM values are within the range found in other theoretical analyses, for instance, 103 MeV/c and 107 MeV/c when describing the stripping mechanism of  ${}^8\text{B}$  breakup on  ${}^{12}\text{C}$  target (denoted KDe and KDp in Ref. [23]), 55 MeV/c and 61 MeV/c FWHM from the analysis of  ${}^8\text{B}$  breakup on  ${}^{197}\text{Au}$  target [22], and width of about 100 MeV/c of the momentum distribution of  ${}^7\text{Be}$  fragments from the breakup of  ${}^8\text{B}$  on  ${}^9\text{Be}$  target [22] when a stripping model [24] was employed.

Here we would like to discuss shortly the applicability of HEA to energies considered in the breakup processes. As known generally, the HEA is applied to energies larger than 100 MeV/nucleon. However, in the last years the HEA was modified and applied also to lower energies (see, e.g., Refs. [40, 51, 63, 64, 52, 65, 66, 67, 35, 36]). The prescription to calculate the profile function in this case consists in a replacement of the straight-line trajectory impact parameter ( $b$ ) by the distance of the closest approach ( $b_c$ ) in the Coulomb field, or by the respective distance ( $r_{cn}$ ) in the presence of nuclear field (ReOP). Recently, the eikonal description of the breakup of exotic nuclei has been developed at low energies by including the Coulomb deflection of the projectile off the target [68, 69]. In principle, this correction is based on the same replacement of the impact parameter  $b$  by  $b_c$  mentioned above and the results obtained in Ref. [69] for the breakup of  ${}^{15}\text{C}$  on Pb at 20 MeV/nucleon confirm the ability of the eikonal approximation to be reliably extended to low energies.

Concerning the use of HEA in the present work, we should note that the fragment-folding potentials  $W_i(r)$  in Eq. (11) are rather deep since they are proportional to the number of nucleons in the target- and fragment-nucleus with radii  $R_t$  and  $R_i$ , respectively. Therefore, a very strong absorption takes place at  $r < R = R_t + R_i$ , and so only the surface region of  $W$  plays decisive role in the process. Thus, the condition for applicability of the eikonal approach can be estimated as  $EA_i \gg W(r \cong R_t + R_i)$  ( $E$  being energy per nucleon) that is fulfilled in our calculations.

In the end, we note that from the comparison of the results in the present work with those obtained in our previous works [38, 39] for the cases of  ${}^{11}\text{Li}$  and  ${}^{11}\text{Be}$  breakup, it can be concluded that the halo cluster ( $2n$  or  $n$ ) in these nuclei can be found outside the core with larger probability than the valence proton in  ${}^8\text{B}$ . This observation together with the variation of the width with target in breakup reactions of  ${}^8\text{B}$  at almost equal energies show the specific features of the momentum distributions of corelike fragments in breakup of neutron and proton halo nuclei.

## 4 Summary and conclusions

In the present work we performed microscopic calculations of the optical potentials and cross sections of elastic scattering  ${}^8\text{B}+{}^{12}\text{C}$  at 25.8 MeV,  ${}^8\text{B}+{}^{58}\text{Ni}$  at 20.7, 23.4, 25.3, 27.2, and 29.3 MeV, and  ${}^8\text{B}+{}^{208}\text{Pb}$  at 170.3 MeV, in comparison with the available experimental data. The direct and exchange isoscalar and isovector parts of the real OP ( $V^{DF}$ ) were calculated microscopically using the double-folding procedure and density dependent M3Y (CDM3Y6-type) effective interaction based on the Paris  $NN$  potential. The imaginary part of the OP ( $W^H$ ) was calculated as a folding integral that corresponds to the one in a phase of HEA and also in a form of the microscopically calculated ReOP ( $W = V^{DF}$ ), where antisymmetrization is taken into account. Two model microscopic densities of protons and neutrons in  ${}^8\text{B}$  were used in the calculations:

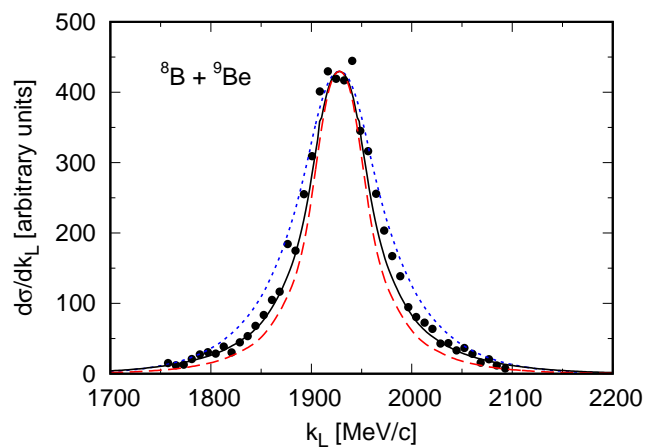


**Fig. 9.** Cross section of stripping reaction in  ${}^8\text{B}+{}^9\text{Be}$  scattering at  $E=41$  MeV/nucleon. Experimental data are taken from Ref. [22].

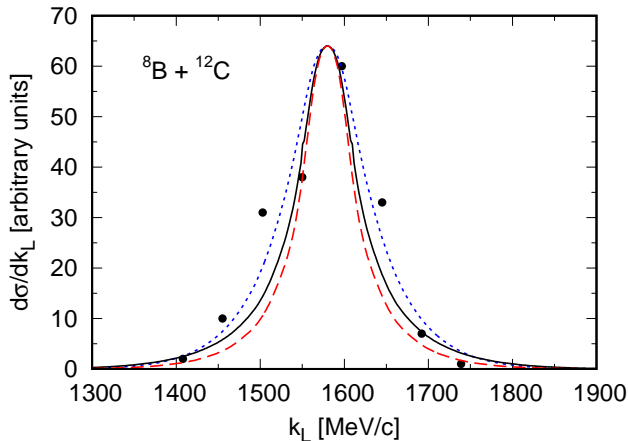


**Fig. 10.** Cross section of stripping reaction in  ${}^8\text{B}+{}^{12}\text{C}$  scattering at  $E=36$  MeV/nucleon. Experimental data are taken from Ref. [23].

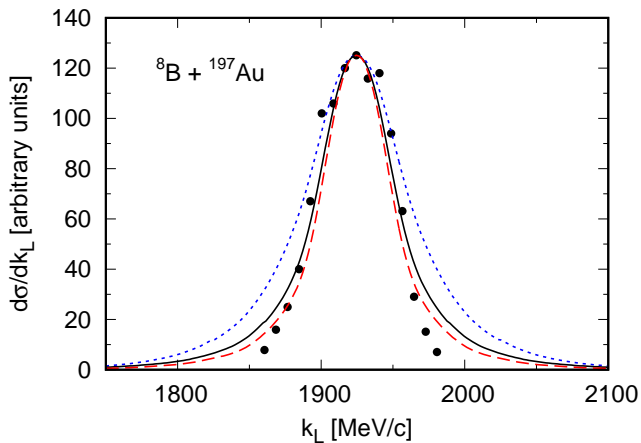


**Fig. 11.** Cross section of stripping reaction in  ${}^8\text{B}+{}^{197}\text{Au}$  scattering at  $E=41$  MeV/nucleon. Experimental data are taken from Ref. [22].

**Table 5.** The values of theoretical and experimental FWHM for stripping mechanism of the  ${}^8\text{B}$  breakup on  ${}^9\text{Be}$ ,  ${}^{12}\text{C}$ , and  ${}^{197}\text{Au}$  targets (in MeV/c) at incident energy  $E=41$ , 36, and 41 MeV/nucleon, respectively. The order of the results for FWHM obtained in this work corresponds to the blue dotted, black solid, and red dashed lines given in Figs. 9, 10, and 11 and rms radii listed in Table 4.

Process	Present work	Exp.
${}^8\text{B}+{}^9\text{Be}$	95.55	$81 \pm 4$
	72.07	
	63.21	
${}^8\text{B}+{}^{12}\text{C}$	108.71	$124 \pm 17$
	81.91	
	70.02	
${}^8\text{B}+{}^{197}\text{Au}$	79.64	$62 \pm 3$
	61.14	
	54.86	

the density calculated within the VMC model [45, 46] and from the three-cluster model [47]. The nucleon density distributions of  ${}^{12}\text{C}$  [56],  ${}^{58}\text{Ni}$  [41], and  ${}^{208}\text{Pb}$  [57] were taken as defolded charge densities obtained from the best fit to the experimental form factors from electron elastic scattering on these nuclei. The elastic scattering differential cross sections and total reaction cross sections were calculated using the program DWUCK4 [55]. In this way, in contrast to the phenomenological and semi-microscopic models we deal with a fully microscopic approach as a physical ground to account for the single-particle structure of the colliding nuclei.

It turned out that the values of the coefficients  $N_R$  and  $N_I$  in Eq. (1) that renormalize the ReOP and ImOP depend on the density of  ${}^8\text{B}$  used in the calculations. The use of the VMC and 3CM densities leads to good agreement with the experimental cross sections. An unambiguous determination of  $N_R$  and  $N_I$  of our microscopic OP, especially if one analyzes the reaction  ${}^8\text{B}+{}^{58}\text{Ni}$ , can be achieved when a simultaneous fit to all data corresponding to different reaction mechanisms is performed [59]. The analysis of the behavior of VMC and 3CM densities and the corresponding OPs (see Fig. 6) in comparison with the fitted WS OP from Ref. [29], as well as our results shown in Fig. 7 give additional information on the decisive role of the nuclear surface on the mechanism of the considered scattering processes.

We have tested our microscopic model studying the role of the breakup mechanism to analyze properly the whole picture of  ${}^8\text{B}$  scattering. For this purpose, we use another folding approach to consider the  ${}^8\text{B}$  breakup by means of the simple  ${}^7\text{Be}+p$  cluster model for the structure of  ${}^8\text{B}$ . We calculate in HEA the ImOP of the interaction of  ${}^7\text{Be}$  with the target, as well as the  $p$ -target interaction. Using them the corresponding  $S$ -matrices for the core and proton within the eikonal formalism are obtained. The latter are used to get results for the longitudinal momentum distributions of  ${}^7\text{Be}$  fragments produced in the breakup of  ${}^8\text{B}$  on different targets. This includes the breakup reactions of  ${}^8\text{B}$  on  ${}^9\text{Be}$  and  ${}^{197}\text{Au}$  at  $E = 41$  MeV/nucleon and  ${}^8\text{B}$  on  ${}^{12}\text{C}$  at  $E = 36$  MeV/nucleon, for which a good agreement of our calculations for the stripping reaction cross sections with the available experimental data were obtained. The theoretical widths are close to the empirical ones.

In general, we can conclude that our microscopic approach can be applied to reaction studies with exotic nuclei such as  ${}^8\text{B}$ . The consistency of our results with the measured elastic cross sections and narrow longitudinal momentum distributions may provide supplemental information on the internal spatial structure of the  ${}^8\text{B}$  nucleus supporting its proton-halo nature.

The authors are grateful to S.C. Pieper for providing with the density distributions of  ${}^8\text{B}$  nucleus calculated within the VMC method and to S.L. Jin for the experimental longitudinal momentum distributions of  ${}^7\text{Be}$  fragments from the breakup of  ${}^8\text{B}$  on a carbon target. The work is partly supported by the Project from the Agreement for co-operation between the INRNE-

BAS (Sofia) and JINR (Dubna). Four of the authors (D.N.K., A.N.A., M.K.G. and K.S.) are grateful for the support of the Bulgarian Science Fund under Contract No. DFNI-T02/19 and one of them (D.N.K.) under Contract No. DFNI-E02/6.

## References

1. I. Tanihata, H. Hamagaki, O. Hashimoto, S. Nagamiya, Y. Shida, N. Yoshikawa, O. Yamakawa, K. Sugimoto, T. Kobayashi, D.E. Greiner, N. Takahashi, Y. Nojiri, *Phys. Lett. B* **160**, 380 (1985).
2. I. Tanihata, H. Hamagaki, O. Hashimoto, Y. Shida, N. Yoshikawa, K. Sugimoto, O. Yamakawa, T. Kobayashi, N. Takahashi, *Phys. Rev. Lett.* **55**, 2676 (1985).
3. P.G. Hansen, A.S. Jensen, B. Jonson, *Annu. Rev. Nucl. Part. Sci.* **45**, 591 (1995).
4. I. Tanihata, *J. Phys. G* **22**, 157 (1996).
5. B. Jonson, *Phys. Rep.* **389**, 1 (2004).
6. G. Baur, K. Hencken, D. Trautmann, *Prog. Part. Nucl. Phys.* **51**, 487 (2003).
7. P.G. Hansen, B. Jonson, *Europhys. Lett.* **4**, 409 (1987).
8. B. Davids, D.W. Anthony, Sam M. Austin, D. Bazin, B. Blank, J.A. Caggiano, M. Chartier, H. Esbensen, P. Hui, C.F. Powell, H. Scheit, B.M. Sherrill, M. Steiner, P. Thirolf, J. Yurkon, A. Zeller, *Phys. Rev. Lett.* **81**, 2209 (1998).
9. B. Davids, S. Typel, *Phys. Rev. C* **68**, 045802 (2003).
10. L. Trache, A. Azhari, F. Carstoiu, H.L. Clark, C.A. Gagliardi, Y.-W. Lui, A.M. Mukhamedzhanov, X. Tang, N. Timofeyuk, R.E. Tribble, *Phys. Rev. C* **67**, 062801 (2003).
11. I. Tanihata, T. Kobayashi, O. Yamakawa, S. Shimoura, K. Ekuni, K. Sugimoto, N. Takahashi, T. Shimoda, H. Sato, *Phys. Lett. B* **206**, 592 (1988).
12. M.M. Obuti, T. Kobayashi, D. Hirata, Y. Ogawa, A. Ozawa, K. Sugimoto, I. Tanihata, D. Olson, W. Christie, H. Wieman, *Nucl. Phys. A* **609**, 74 (1996).
13. J.S. Wang, W.Q. Shen, Z.Y. Zhu, J. Feng, Z.Y. Guo, W.L. Zhan, G.Q. Xiao, X.Z. Cai, D.Q. Fang, H.Y. Zhang, Y.G. Ma, *Nucl. Phys. A* **691**, 618 (2001).
14. F. Negoita *et al.*, *Phys. Rev. C* **54**, 1787 (1996).
15. M. Fukuda *et al.*, *Nucl. Phys. A* **656**, 209 (1999).
16. R.E. Warner *et al.*, *Phys. Rev. C* **52**, R1166 (1995).
17. B. Blank *et al.*, *Nucl. Phys. A* **624**, 242 (1997).
18. M.H. Smedberg *et al.*, *Phys. Lett. B* **452**, 1 (1999).
19. T. Minamisono *et al.*, *Phys. Rev. Lett.* **69**, 2058 (1992).
20. T. Sumikama *et al.*, *Phys. Rev. C* **74**, 024327 (2006).
21. W. Schwab, H. Geissel, H. Lenske, K.-H. Behr, A. Brünle, K. Burkard, H. Irnich, T. Kobayashi, G. Kraus, A. Magel, G. Münzenberg, F. Nickel, K. Riisager, C. Scheidenberger, B.M. Sherrill, T. Suzuki, B. Voss, *Z. Phys. A* **350**, 283 (1995).
22. J.H. Kelley, Sam M. Austin, A. Azhari, D. Bazin, J.A. Brown, H. Esbensen, M. Fauerbach, M. Hellström, S.E. Hirzebruch, R.A. Kryger, D.J. Morrissey, R. Pfaff, C.F. Powell, E. Ramakrishnan, B.M. Sherrill, M. Steiner, T. Suomijärvi, M. Thoennessen, *Phys. Rev. Lett.* **77**, 5020 (1996).
23. S.L. Jin *et al.*, *Phys. Rev. C* **91**, 054617 (2015).
24. H. Esbensen, *Phys. Rev. C* **53**, 2007 (1996).
25. B. Abu-Ibrahim, Y. Ogawa, Y. Suzuki, I. Tanihata, *Comput. Phys. Comm.* **151**, 369 (2003).
26. L.V. Grigorenko, B.V. Danilin, V.D. Efros, N.B. Shulgina, M.V. Zhukov, *Phys. Rev. C* **57**, R2099 (1998).
27. F. Carstoiu, L. Trache, C.A. Gagliardi, R.E. Tribble, A.M. Mukhamedzhanov, *Phys. Rev. C* **63**, 054310 (2001).
28. A. Barioni, J.C. Zamora, V. Guimarães, B. Paes, J. Lubian, E.F. Aguilera, J.J. Kolata, A.L. Roberts, F.D. Becchetti, A. Villano, M. Ojaruega, H. Jiang, *Phys. Rev. C* **84**, 014603 (2011).
29. E.F. Aguilera, E. Martinez-Quiroz, D. Lizcano, A. Gómez-Camacho, J.J. Kolata, L.O. Lamm, V. Guimarães, R. Lichtenhåler, O. Camargo, F.D. Becchetti, H. Jiang, P.A. DeYoung, P.J. Mears, T.L. Belyaeva, *Phys. Rev. C* **79**, 021601(R) (2009).
30. Y.Y. Yang *et al.*, *Phys. Rev. C* **87**, 044613 (2013).
31. B. Paes, J. Lubian, P.R.S. Gomes, V. Guimarães, *Nucl. Phys. A* **890-891**, 1 (2012).
32. J. Lubian, T. Correa, E.F. Aguilera, L.F. Canto, A. Gómez-Camacho, E.M. Quiroz, P.R.S. Gomes, *Phys. Rev. C* **79**, 064605 (2009).
33. F.M. Nunes, I.J. Thompson, *Phys. Rev. C* **57**, R2818 (1998).
34. B. Mukeru, M.L. Lekala, A.S. Denikin, *Nucl. Phys. A* **935**, 18 (2015).
35. K.V. Lukyanov, V.K. Lukyanov, E.V. Zemlyanaya, A.N. Antonov, M.K. Gaidarov, *Eur. Phys. J. A* **33**, 389 (2007).
36. V.K. Lukyanov, E.V. Zemlyanaya, K.V. Lukyanov, D.N. Kadrev, A.N. Antonov, M.K. Gaidarov, S.E. Massen, *Phys. Rev. C* **80**, 024609 (2009).
37. V.K. Lukyanov, D.N. Kadrev, E.V. Zemlyanaya, A.N. Antonov, K.V. Lukyanov, M.K. Gaidarov, *Phys. Rev. C* **82**, 024604 (2010).
38. V.K. Lukyanov, E.V. Zemlyanaya, K.V. Lukyanov, D.N. Kadrev, A.N. Antonov, M.K. Gaidarov, K. Spasova, *Phys. Rev. C* **88**, 034612 (2013); *Phys. At. Nucl.* **75**, 1407 (2012).
39. V.K. Lukyanov, D.N. Kadrev, E.V. Zemlyanaya, K. Spasova, K.V. Lukyanov, A.N. Antonov, M.K. Gaidarov, *Phys. Rev. C* **91**, 034606 (2015).
40. K.V. Lukyanov, E.V. Zemlyanaya, V.K. Lukyanov, JINR Preprint P4-2004-115, Dubna, 2004; *Phys. At. Nucl.* **69**, 240 (2006).
41. D.T. Khoa, G.R. Satchler, *Nucl. Phys. A* **668**, 3 (2000).
42. K.V. Lukyanov, JINR Comm. R11-2007-38, Dubna, 2007.
43. R.J. Glauber, in *Lectures in Theoretical Physics* (New York, Interscience, 1959), p.315.
44. A.G. Sitenko, *Ukr. Fiz. J.* **4**, 152 (1959).
45. J. Carlson, S. Gandolfi, F. Pederiva, S.C. Pieper, R. Schiavilla, K.E. Schmidt, R.B. Wiringa, *Rev. Mod. Phys.* **87**, 1067 (2015).
46. S.C. Pieper, private communication.
47. K. Varga, Y. Suzuki, I. Tanihata, *Phys. Rev. C* **52**, 3013 (1995).
48. G.R. Satchler, W.G. Love, *Phys. Rep.* **55**, 183 (1979); G.R. Satchler, *Direct Nuclear Reactions* (Clarendon Press, Oxford, UK, 1983).
49. M. Avrigeanu, G.S. Anagnostatos, A.N. Antonov, J. Giapitzakis, *Phys. Rev. C* **62**, 017001 (2000); M. Avrigeanu, G.S. Anagnostatos, A.N. Antonov, V. Avrigeanu, *Int. J. Mod. Phys. E* **11**, 249 (2002); M. Avrigeanu, A.N. Antonov, H. Lenske, I. Stetcu, *Nucl. Phys. A* **693**, 616 (2001).
50. J.W. Negele, D. Vautherin, *Phys. Rev. C* **5**, 1472 (1972).
51. P. Shukla, *Phys. Rev. C* **67**, 054607 (2003).
52. S. Charagi, G. Gupta, *Phys. Rev. C* **41**, 1610 (1990); **46**, 1982 (1992).
53. P. Shukla, arXiv:nucl-th/0112039.

54. C. Xiangzhou, F. Jun, S. Wenqing, M. Yugang, W. Jiansong, Y. Wei, *Phys. Rev. C* **58**, 572 (1998).
55. P.D. Kunz, E. Rost, in *Computational Nuclear Physics*, edited by K. Langanke *et al.* (Springer-Verlag, New York, 1993), Vol. 2, p. 88.
56. V.V. Burov, V.K. Lukyanov, Preprint JINR, R4-11098, 1977, Dubna; V.V. Burov, D.N. Kadrev, V.K. Lukyanov, Yu.S. Pol', *Phys. At. Nucl.* **61**, 525 (1998); V.K. Lukyanov *et al.*, *Phys. At. Nucl.* **67**, 1282 (2004).
57. J.D. Patterson, R.J. Peterson, *Nucl. Phys. A* **717**, 235 (2003).
58. L.C. Chamon, B.V. Carlson, L.R. Gasques, D. Pereira, C. De Conti, M.A.G. Alvarez, M.S. Hussein, M.A. Cândido Ribeiro, E.S. Rossi, C.P. Silva, *Phys. Rev. C* **66**, 014610 (2002).
59. A. Gómez Camacho, E.F. Aguilera, P.R.S. Gomes, J. Lubian, *Phys. Rev. C* **84**, 034615 (2011).
60. K. Hencken, G. Bertsch, H. Esbensen, *Phys. Rev. C* **54**, 3043 (1996).
61. V.I. Kovalchuk, *Phys. At. Nucl.* **72**, No.8, 1247 (2009).
62. I. Pecina *et al.*, *Phys. Rev. C* **52**, 191 (1995).
63. K.M. De Vries, J.C. Peng, *Phys. Rev. C* **22**, 1055 (1980).
64. A. Vitturi, F. Zardi, *Phys. Rev. C* **36**, 1404 (1987).
65. S.K. Charagi, S.K. Gupta, *Phys. Rev. C* **56**, 1171 (1997).
66. D.M. Brink, G.R. Satchler, *J. Phys. G* **7**, 43 (1981).
67. A. de Vismes, P. Roussel-Chomaz, F. Carstoiu, *Phys. Rev. C* **62**, 064612 (2000).
68. T. Fukui, K. Ogata, P. Capel, *Phys. Rev. C* **90**, 034617 (2014).
69. P. Capel, F. Colomer, H. Esbensen, T. Fukui, R.C. Johnson, F.M. Nunes, K. Ogata, *J. Phys.: Conf. Ser.* **724**, 012005 (2016).